ASME Journal of Turbomachinery
Online journal at:
https://asmedigitalcollection.asme.org/turbomachinery

Robert Schaffrath[1]
Institute of Low-Carbon Industrial Processes,
German Aerospace Center,
Äußere Oybiner Str. 14/16,
02763 Zittau, Germany
e-mail: robert.schaffrath@dlr.de

Eberhard Nicke
Institute of Low-Carbon Industrial Processes,
German Aerospace Center,
Äußere Oybiner Str. 14/16,
02763 Zittau, Germany
e-mail: eberhard.nicke@dlr.de

Nicolai Forsthofer
Institute of Structures and Design,
German Aerospace Center,
Pfaffenwaldring 38–40,
70569 Stuttgart, Germany
e-mail: nicolai.forsthofer@dlr.de

Oliver Kunc
Institute of Structures and Design,
German Aerospace Center,
Pfaffenwaldring 38–40,
70569 Stuttgart, Germany
e-mail: oliver.kunc@dlr.de

Christian Voß
Institute of Propulsion Technology,
German Aerospace Center,
Äußere Oybiner Str. 14/16,
02763 Zittau, Germany
e-mail: christian.voss@dlr.de

Gradient-Free Aerodynamic Optimization With Structural Constraints and Surge Line Control for Radial Compressor Stage

The concept and design of high-temperature heat pumps (HTHP) including their components for specific temperature needs is a time-consuming and interdisciplinary task. Especially, the design of compressor geometries have a big impact on the overall performance and the initial costs of the system. For this reason, in this work, an automated aerodynamic gradient-free optimization including structural constraints for the geometry of a radial compressor impeller blade as well as diffusor vane geometry for water steam, that is applied in a reverse Rankine cycle-based HTHP, is presented. The objective of the optimization is the isentropic efficiency in the aerodynamic design point (ADP) of the compressor. The requirements for the cycle simulation of the whole HTHP system and structural needs are satisfied by constraints for pressure ratio, mass flowrate, and limits for stresses in the blade and disk geometry. The optimization method is based on evolutionary algorithms and stochastical surrogate models. Additionally, a highly throttled operating point is regarded to achieve an acceptable distance to the surge line. These types of optimization problems are often characterized by many unconverged iterations due to unstable computational fluid dynamic (CFD) simulations. To encounter this, a study of the optimization process with different surrogate models is presented. The results are discussed with respect to convergence history as well as objective and constraint improvement. [DOI: 10.1115/1.4067687]

Keywords: radial compressor, aero-structure optimization, water steam, centrifugal compressors and pumps, computational fluid dynamics (CFD), turbomachinery blading design

1 Introduction

Global warming is one of the key challenges of the 21st century with wide-ranging impact on ecosystems as well as human systems [1]. Especially, the industrial sector is responsible for almost 25% of greenhouse gas emissions. Besides reducing the usage of primary energy sources, the reuse of waste heat is key for achieving reduction targets. The investigation of high-temperature heat pumps (HTHP) is a promising approach to achieve a leap-frogging step in the decarbonization of industrial processes. One of the key components of a high-temperature heat pump is the compressor. In many heat pump systems with heat sink temperatures below 100 °C, displacement compressor systems are used. However, turbocompressors are a promising alternative due to higher efficiencies and the ability to operate at high-pressure ratios [2,3]. Especially for the application of heat pump systems in industrial processes, the demand for optimized compressors is rising. In the case of medium-sized systems, centrifugal compressors are suitable due to higher pressure ratios and lower mass flowrates (Cordier diagram [4]).

The optimization of a radial compressor is an interdisciplinary task because of aerodynamic and structural-mechanical requirements, manufacturing limitations, and demands on acceptable operating range. Furthermore, the aerodynamic evaluation of compressor geometries with computational fluid dynamic (CFD) methods is very time-consuming; thus, high-performance computing systems are needed.

Besides the operating efficiency, the pressure ratio requirements for the specific application defines the design objectives of turbocompressors. Because of that, many optimization problems are either constrained by pressure ratio limitations or the pressure ratio is one of the objectives. This leads to shifted aerodynamic design points near the surge line in the performance map of the compressor. To counter this, different strategies can be found in the literature. A common way is to regard a highly throttled

[1]Corresponding author.

Contributed by International Gas Turbine Institute (IGTI) of ASME for publication in the Journal of Turbomachinery. Manuscript received July 11, 2023; final manuscript received March 27, 2024; published online February 18, 2025. Tech. Editor: David G. Bogard.

Copyright © 2025 by ASME; reuse license CC-BY 4.0

operating point (HTOP) near the surge line during the optimization [5,6]. By using that operating point, it is possible to define the Cumpsty margin, which is a measure of the distance between the ADP and the surge line. This can be used during the optimization to generate geometries that have a specific distance to the surge line [7]. Otherwise, if the distance is not directly necessary, the highly throttled operating point achieves optimization results that are not located at unstable operating conditions. Another approach is presented by Ratz et al. [8] by using local flow parameters to define an objective function for the surge margin, that does not need a highly throttled operating point during the optimization. The advantage is a more stable optimization process, but the initial computational cost is higher because of preliminary surge line calculations. It could be shown, that the optimization result with an objective function based on flow parameters is comparable to a common approach with a highly throttled operating point. Similar suggestions can be found in Refs. [9,10].

The greater number of optimization parameters of the compressor geometry requires an automated optimization process. Gradient-based and gradient-free methods could be successfully applied to radial compressor optimization tasks [11–13]. The advantage of gradient-free methods is that they are suitable to reach a global optimum and can handle nondifferentiable objectives and even unconverged simulations but suffer from the number of objective evaluations. In contrast, gradient-based methods require fewer objective evaluations because of derivative information but will most likely converge to a local minimum. In their work, Hottois et al. [14] showed by applying a gradient-free and a gradient-based optimization on a turbine vane that both methods revealed similar results. Nevertheless, their findings also proved that gradient-based methods can reach the global optimum in the case of highly complex optimization problems. To accelerate gradient-free methods, surrogate models are commonly used [12,13,15]. The general idea of a surrogate model is to use information based on already successfully calculated compressor geometries and create a fast-to-evaluate mathematical function for the objective. Now the algorithm can be used to run the optimization with the surrogate model instead of the complex and exact compressor evaluation. Nowadays, Kriging-based methods (also known as Gaussian process regression) are frequently used as surrogate models. The Kriging surrogate model can be evaluated in different ways. The most common infill criterion is expected improvement and prediction minimization, which is also known as volume gain in the literature. A third way is entropy maximization, but this is a less frequent application of that method, because of the very explorative character and so it is used effectively only in the beginning of an optimization. Another surrogate model is neural gas, based on self-organizing maps, that can be used to predict well-performing geometries. Further information can be found in Refs. [16–18].

During an optimization, it is possible to use different infill criteria. In the literature, we could find only one publication with such an optimization methodology [16]. Aissa and Verstraete presented a gradient-free aero-structure optimization with alternating infill criteria with expected improvement and prediction minimization. The application was a radial compressor impeller geometry. But so far, to the best knowledge of the authors, a comprehensive study of different infill criteria during an aerodynamic optimization with the goal of finding optimal combinations is an innovative investigation. Probable causes are, on the one hand, side the enormous amount of cluster contingent to run an optimization multiple times with different infill criteria and, on the other hand, the sparse availability of different surrogate models implemented in the used design suites.

The structure of the article is as follows: the following section presents the optimization methodology and the parametrization of the compressor geometry. Furthermore, details of the meshing process, CFD calculations, computational structure mechanics (CSM) calculations and post-processing of the data will be presented. The third section gives an overview of the applied surrogate models and infill criteria. The next section presents the optimization results. This is followed by comparing the baseline and optimized geometry. Finally, an automatic hyperparameter tuning (AHPT) is carried out.

2 Optimization Methodology

For solving the optimization problem, AutoOpti is used, see Refs. [12,19]. It implements a gradient-free evolutionary algorithm accelerated with different surrogate models and infill criteria. The evaluation of geometries during each iteration step is enabled by a user-defined process chain. AutoOpti is highly parallelized by multiple process chain evaluations at the same time, with the goal of fast optimization convergence. The general optimization procedure is shown in Fig. 1. The optimization is initiated with a randomly sampled database, followed by the training of surrogate models. Surrogate models that are implemented in AutoOpti includes Kriging approximation and neural gas. Furthermore, infill criteria implemented for Kriging approximation are expected improvement and prediction minimization. An overview of the surrogate models and criteria will be given in Sec. 3. After successful training of surrogate models, an infill criterion is selected, which is subsequently implemented by randomized selection with user-defined probabilities for each infill criteria. By using that procedure, it is possible to combine exploitative and explorative system behavior. The next steps describe the geometry parametrization of the impeller and diffusor and CFD as well as CSM evaluation. Details are given in Sec. 2.1. After successful process chain evaluations, the convergence criteria are checked. We are using a maximum number of successful process chain evaluations and a time limit for terminating the optimization process.

2.1 Parametrization. The first step of the geometry parametrization is the flow path, which is designed by a hub and shroud curve in the meridional plane (Fig. 2). Impeller and diffusor are located inside the flow path and are visualized with a black mesh. In order to modify the flow path of the compressor, the hub and shroud curve are splined by control points. The first and second control points for the shroud curve are used to modify the impeller inlet diameter. The first free variable #1 is used for both control points to achieve a straight inlet, by modifying the radial component. The next three control points are individually shifted in the normal direction from hub to shroud by free variables #2–#4. Because of the big influence of the flow path along the impeller length of the ADP, three control points are used. For simplifying the manufacturing of the diffusor area, a constant shroud contour is preferred. For the realization, six control points are included with an axial degree of freedom, that are controlled by free variable

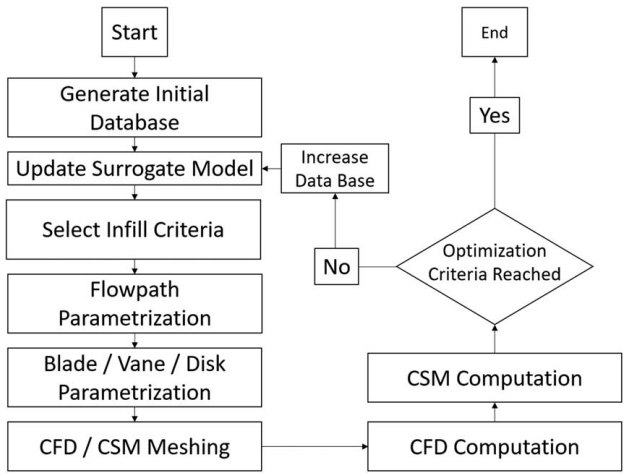

Fig. 1 Schematic overview of optimization methodology

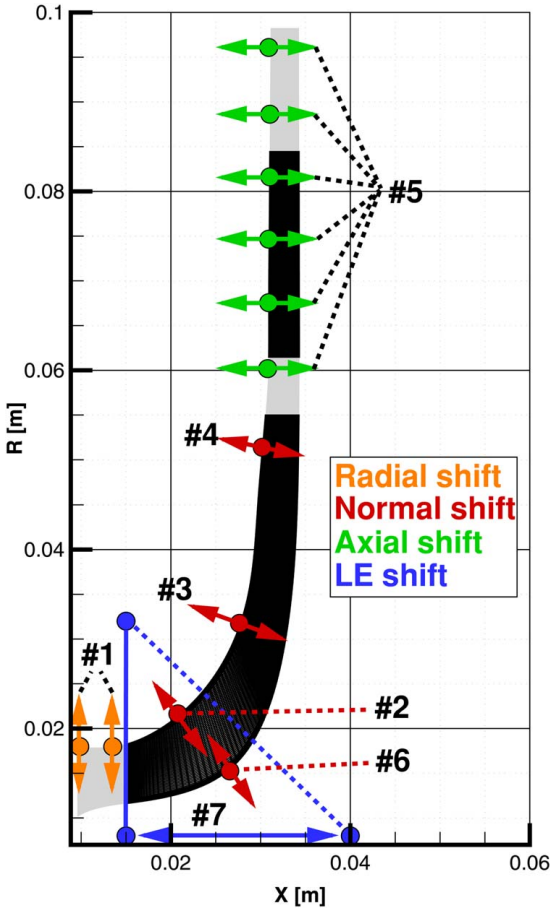

Fig. 2 Parametrization of flow path in meridional plane

#5. In contrast, the hub curve is only parametrized by one free variable #6, because of the reduction of free variables. The location of the control point is within the area of highest curvature, because of the biggest influence in aero- and structural mechanics and can be shifted in an orthogonal direction to the hub curve.

With defined flow path shifts, the parametrization of blade and vane can be conducted. The first step is the parametrization of the leading edge of the blade (Fig. 3). In the literature, comparable radial compressor impeller optimization has shown that huge geometry modifications of the leading edge can occur during an automated optimization [6,12]. Because of that, five equally distributed control points for the parametrization of the leading edge are used. For each of these control points, free variables #8–#12 for the axial shift are applied. Furthermore, an overall shift in the meridional plane of the leading edge is regarded by free variable #7, by modifying the slope of the blue dashed line (Fig. 2). By using that scheme, the limit of free variables #8–#12 can be reduced, due to the overall shift by free variable #7. This kind of scheme should result in a more stable blade parametrization.

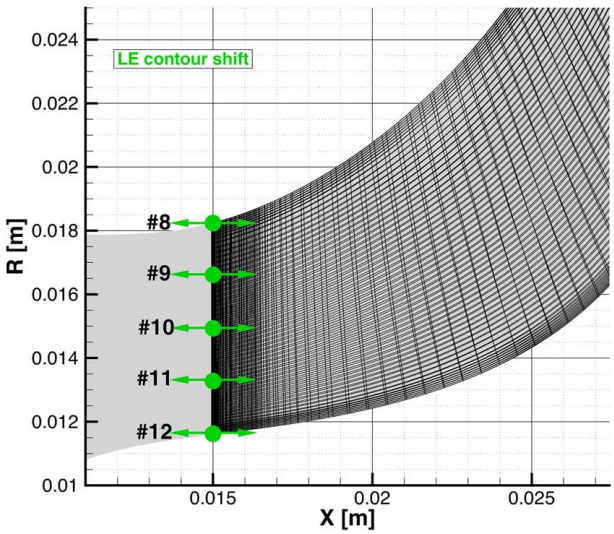

Fig. 3 Parametrization of leading edge contour by control points in meridional plane

The shape of the blade camber line is designed by a distribution of β angle in (m', θ) coordinate system. The angle β is defined as the angle between the meridional plane and S, that is calculated by integration of ds, which is:

$$\mathrm{d}s = \sqrt{(\mathrm{d}x)^2 + (\mathrm{d}r)^2 + (r\mathrm{d}\theta)^2} \tag{1}$$

The meridional plane is defined by the arc length

$$\mathrm{d}m = \sqrt{(\mathrm{d}x)^2 + (\mathrm{d}r)^2} \tag{2}$$

and m' can be defined as differential normalized arc length with respect to the impeller radius r in the meridional plane by

$$\mathrm{d}m' = \frac{\mathrm{d}m}{r} \tag{3}$$

With the notation defined previously, the β angle can be defined as

$$\tan\beta = \frac{r\mathrm{d}\theta}{\mathrm{d}m} \tag{4}$$

The definition of β, S, m, and θ can be seen in Fig. 4. Further information can be found in Refs. [4,20].

Because of prescribed notations, it is sufficient to define the β angle distribution in (m', θ) coordinate system. Furthermore, the circumferential coordinate θ has to be defined. The blade is defined by two profiles along the span, one located at the hub and the second at the shroud contour. The vane is constant in spanwise direction, to reduce the number of free variables. Due to the strong impact of the blade on the overall compressor performance, more free variables are defined for parametrization. The circumferential coordinate for the hub profile of the blade is defined as free variable #13, the shroud profile is free variable #14, and the vane profile is free variable #40. For each profile, the β angle distribution can be seen in Fig. 5. The shape of the profile is parametrized by

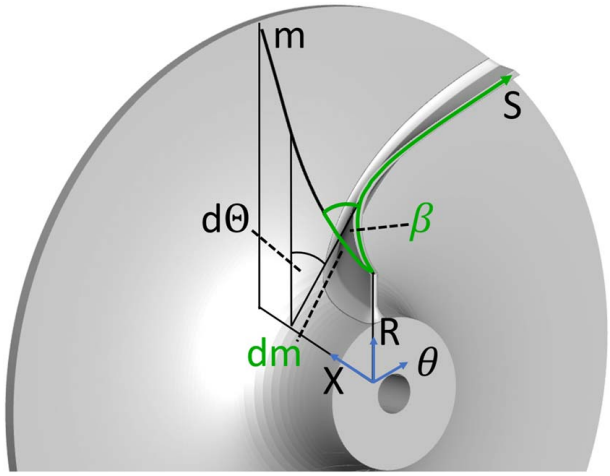

Fig. 4 Definition of β and θ angle

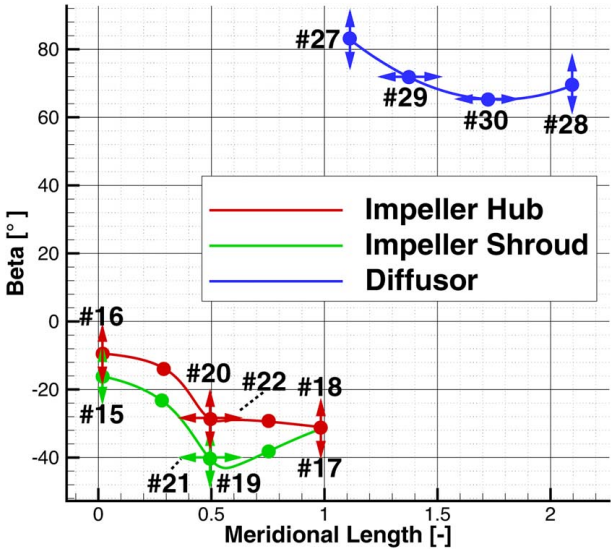

Fig. 5 β angle distribution of blade and vane in meridional plane

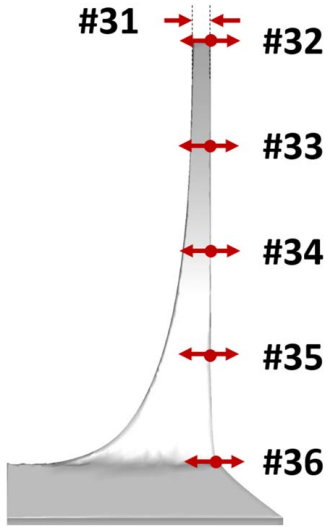

Fig. 7 Parametrization of rear side of disk

control points. The profiles of the blade consist of five and the profile of the vane consists of four control points, respectively. The blade β angle at the leading edge is parametrized by free variables #15 and #16 and at the trailing edge by free variables #17 and #18 for the hub and shroud profile. The meridional coordinate of the second and fourth control points is fixed and the β angle is being derived by the β angle at the leading and trailing edge, respectively, because of continuous and differentiable conditions of the overall profile shape. The meridional coordinate and β angle of the third control point are parametrized for both profiles. The β angles are shifted by free variables #19 and #20 and the meridional coordinate by free variables #21 and #22 in the case of the hub and shroud profile. The choice of the control points and the degrees of freedom is a good compromise between the reduction of the number of free variables and the variability of the blade parametrization. The β angle of the leading and trailing edge of the vane is parametrized by free variable #27 and free variable #28, respectively. The intermediate control points are located at 33% and 66% of vane meridional length. The only degree of freedom is described by the meridional coordinates of the control points, that are parametrized by free variables #29 and #30. Furthermore, blades and vanes that are defined by multiple control points result in wavy geometries with high manufacturing costs.

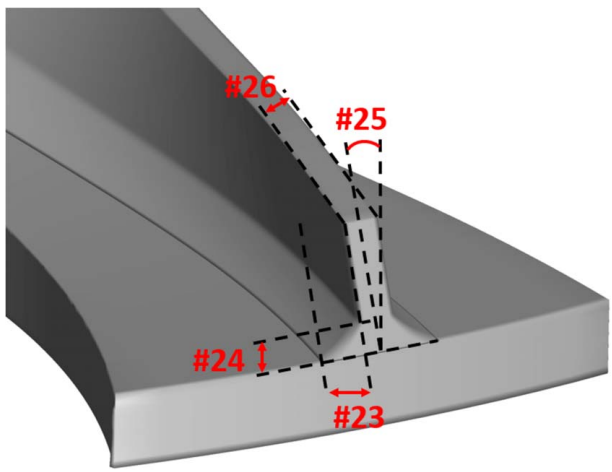

Fig. 6 Definition of rake angle γ, lower blade thickness, and fillet structure

The definition of the rake angle, the free variables of the fillet parametrization, and the thickness of the impeller blade can be seen in Fig. 6. The rake angle is defined by the positive angle between the line, that connects the trailing edge points of both design profiles and the vertical line that intersects the hub profile at the trailing edge location. The rake angle is controlled by the circumferential shift of the shroud profile with free variable #25. The thickness of the blade at the leading edge is kept constant at 1.3 mm. To satisfy structural-mechanical requirements, the blade thickness at the trailing edge position is parametrized by free variable #26. The intermediate thickness is linearly interpolated between the leading and trailing edges. The fillet is designed by two free variables. The first free variable #23 controls the blow curve which is the increased profile at the hub surface, where the smooth connection between blade and disk starts. The blade curve, which is an intermediate profile between hub and shroud profile, is designed by free variable #24. Based on these two profiles, the fillet is designed as a slightly smoothed curve between them. A perfect circular fillet could not be used, since the fillet radii are lower than 1 mm, which results in hard-to-manufacture geometries. The free parameters for fillet design can be seen in Fig. 6.

To satisfy structural-mechanical requirements, it is not only sufficient to consider the blade but also the disk geometry of the radial compressor. The parametrization of the disk is shown in Fig. 7. The overall thickness of the disk is designed by free variable #31. Intermediate shifts of the rear side according to the x direction are controlled by free variables #32–#36. The shift locations start at the radius of the trailing edge of the blade and end at the radius of the leading edge.

Furthermore, the general radii of impeller and diffusor are considered. The parametrization can be seen in Fig. 8. The impeller radius is controlled by free variable #37, the vaneless space by free variable #38, and the radius of the diffusor by free variable #39. Additionally, a constraint is regarded that the vaneless space is always positive and at least 5 mm. Moreover, the location of the mixing plane is always shifted in the middle of the vaneless space. In the same way, the outlet domain is moved right behind the trailing edge.

All of the parametrization of blade geometry is done with the DLR internal tool *BladeGenerator*. The number of blades is being kept at 19 and the number of vanes at 14. For more information, see Ref. [19].

2.2 Computational Fluid Dynamic Mesh Generation and Grid Convergence. For evaluation of compressor performance, a

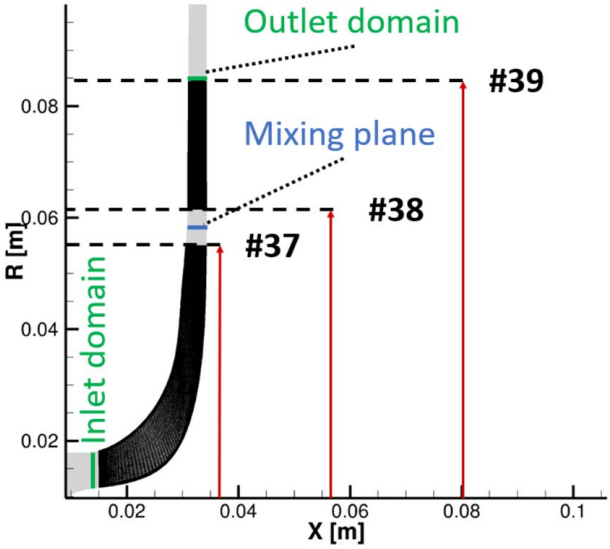

Fig. 8 Definition of diameters of impeller and diffusor

CFD calculation of impeller and diffusor geometry is carried out. Based on the parametrized geometry, the CFD mesh is computed by using a DLR internal meshing tool PyMesh [21]. It implements an O-C-H mesh topology, with shape modifications done by cell spacings, block relationships, and dimensions. Because of the coupled rotor-stator computation, two individual meshes are calculated. The connection is done at the mixing plane (Fig. 8). To run low-Reynolds CFD models, the mesh was iteratively refined. The evaluated $y+$ values at boundaries are below 1. An exception is the tip clearance of the impeller geometry, where wall functions are used to reduce the mesh dimension. The complete compressor mesh is visualized in Fig. 9 and a detailed view of the leading edge mesh is shown in Fig. 10. Both visualizations show the mesh at 50% span.

For proofing the mesh resolution, a grid convergence study is carried out. Therefore, the mesh was coarsened two times with a refinement ratio r of approximately 1.2 in every dimension. The process was done by adapting the major block dimensions and constant near boundary cell spacing to enable successful simulation without the necessity of wall functions, except for the tip clearance. Based on the fact, that only integer numbers of block dimensions are modified, the theoretical refinement ratio of 1.2 could not be reached exactly at some mesh modifications. The CFD simulation is solved on every mesh.

To compare the results to a theoretical on an infinitesimal fine mesh, the method of Richardson extrapolation is applied. The

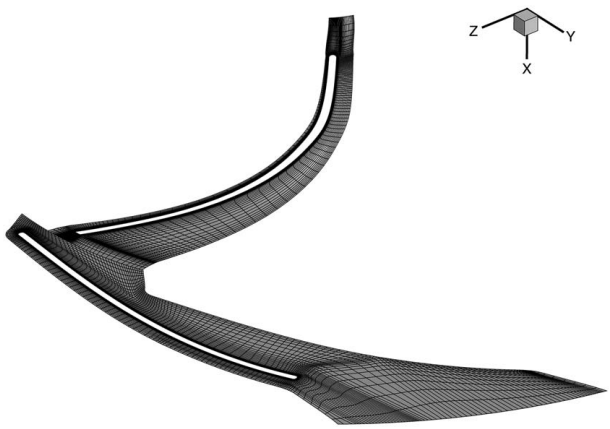

Fig. 9 Finest mesh of impeller and diffusor at midspan

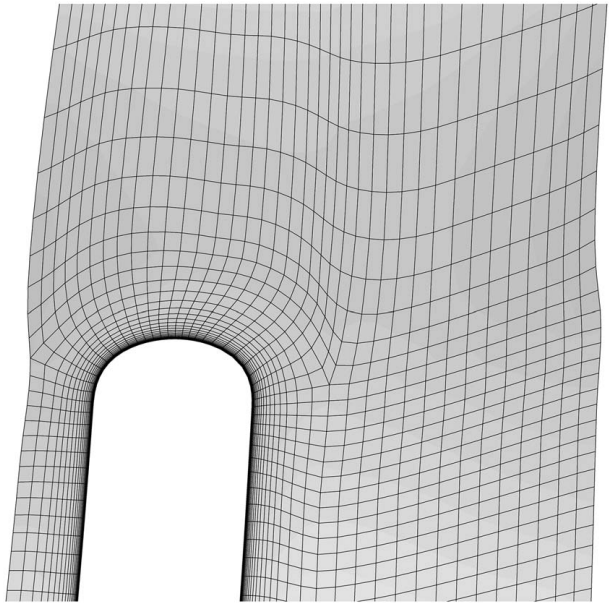

Fig. 10 Finest mesh of impeller leading edge at midspan

theory behind the Richardson extrapolation can be described by the relation $E = C \times h^p$, where E is the error, p is the convergence order, and h is spatial discretization. By applying Taylor approximation, the value of the computed parameter f on an infinitesimal fine mesh $h = 0$ can be calculated by Eq. (5)

$$f_{h=0} = f_{\text{fine}} + \frac{f_{\text{fine}} - f_{\text{medium}}}{r^p - 1}. \tag{5}$$

The calculation of p can be seen in Eq. (6).

$$p = \frac{ln\left(\frac{f_{\text{coarse}} - f_{\text{medium}}}{f_{\text{medium}} - f_{\text{fine}}}\right)}{ln(r)} \tag{6}$$

With the help of the Richardson extrapolation, the error between every solved mesh and the solution on the theoretical infinitesimal fine mesh can be calculated. After that, the grid convergence index (GCI), which is a measure to display the grid quality, can be calculated for refinement steps from *coarse* to *medium* and *medium* to *fine* by

$$\text{GCI}_{\text{coarse, medium}} = \frac{F_s \times \varepsilon_{\text{coarse, medium}}}{r^p - 1} \tag{7}$$

and

$$\text{GCI}_{\text{medium, fine}} = \frac{F_s \times \varepsilon_{\text{medium, fine}}}{r^p - 1} \tag{8}$$

with F_s as a safety factor, which is usually around 1.25 and $\varepsilon_{\text{coarse, medium}}$ and $\varepsilon_{\text{medium, fine}}$ are the relative errors between coarse and medium and medium and fine grid, respectively. Finally, it is possible to ensure, that all grids are in the asymptotic range (AR). That can be done by calculating

$$\text{AR} = \frac{\text{GCI}_{\text{coarse, medium}}}{r^p \times \text{GCI}_{\text{medium, fine}}} \tag{9}$$

For AR, Eq. (9) has to be close to 1.0. The results of the CFD calculations for isentropic efficiency η_{tt} and total to static pressure ratio π_{ts} on every mesh as well as the results of the Richardson extrapolation can be seen in Table 1. Furthermore, the relative error for η_{tt} and π_{ts} between Richardson extrapolation and mesh solution is plotted in Fig. 11. The error of η_{tt} is higher for coarse meshes compared to the error of π_{ts} because of the more complex structure and

Table 1 Results of grid convergence study for radial compressor stage

	# cells	π_{ts}	η_{tt} (%)	Rel. error π_{ts}	Rel. error η_{tt}
Coarse grid	580,944	1.97294	0.68261	0.000968	0.006947
Medium grid	883,932	1.97594	0.67644	0.000553	0.002156
Fine grid	1,413,027	1.97514	0.67762	0.000147	0.000413
Richardson extra.		1.97485	0.67790	0	0

dependencies of the efficiency definition. The corresponding asymptotic ranges are 0.99959 in case of π_{ts} and 1.0017 for η_{tt}. Further information on the Richardson extrapolation and grid convergence studies can be found in Refs. [22,23]. For the optimization, the finest mesh was used.

2.3 Computational Fluid Dynamic Simulation. The performance of the radial compressor stage is carried out by CFD calculation of steady-state Reynolds-averaged Navier–Stokes equation. The inlet and outlet domains can be seen in Fig. 8. Because of the periodicity of the geometry, only one segment is calculated. Therefore, a mixing plane is used between the rotating and stationary stage. For the calculation of the thermodynamic properties of water steam, the ideal gas model is applied. The viscosity is calculated by using the Sutherland model. The influence of the turbulence is considered by the Menter shear stress transport turbulence model. The solver is back-pressure controlled and a second-order spatial discretization scheme is used. At the compressor inlet, the stagnation pressure and stagnation temperature and at the outlet the static pressure are defined, respectively. For successful convergence, the variation of mass flowrate, pressure ratio, and isentropic efficiency between inlet and outlet have to be smaller than 0.0005 for 200 time-steps. The calculation is initialized by a circumferential averaged solution of the baseline geometry. The simulation is conducted by using the solver TRACE [24].

2.4 Computational Structure Mechanics Simulation. For the satisfaction of structural-mechanical requirements, a static CSM simulation for the rotating stage is executed. The meshing process is implemented by using a DLR internal meshing software. The blade and disk geometry are individually discretized by hexahedral mesh and connected by multi-point constraints (MPC). Based on the aerodynamic simulation, the pressure and temperature

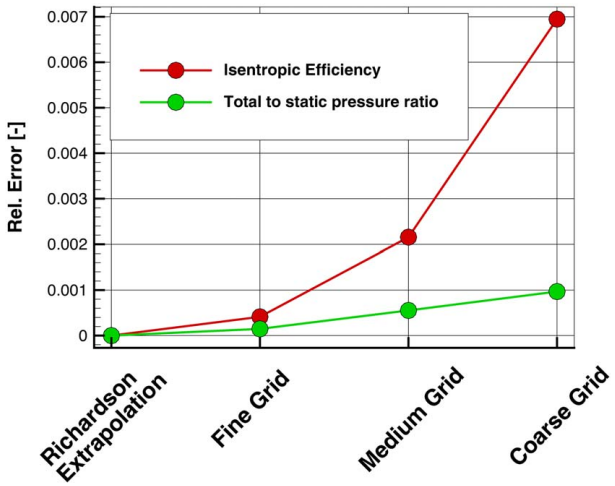

Fig. 11 Relative errors between different mesh resolutions and Richardson extrapolation

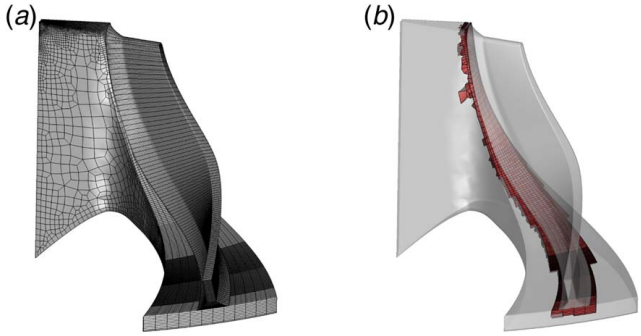

Fig. 12 CSM mesh for blade and disk (*a*) and ignored cells (red) in stress post-processing (*b*)

loads are considered. In addition, the rotation of the geometry is a further mechanical load for the system. By using cyclic boundary conditions, only one blade and disk segment is taken into account. For the solution, the open source solver CALCULIX with compiled solver SPOOLES is applied [25]. Because of the MPC, stresses in the connection area are potentially unreliable. To encounter this, the MPC cells are not taken into account for automatic post-processing during the optimization process. The CSM mesh and the cells, that are neglected in post-processing, are shown in Fig. 12. Besides that, the first 5% of the blade height is neglected to not sophisticate the post-processing process. Preliminary simulations revealed that the maximum stress values are not located in that region; therefore, the limited post-processing has no influence on the final CSM result.

2.5 Objective and Constraints. The optimized compressor geometry will be integrated into an HTHP with water steam as the working fluid. To achieve a high-temperature lift, the heat pump consists of three compressor stages. The goal of the presented optimization methodology is to maximize the efficiency in the ADP of the second stage. Because of already existing performance maps of the first and third stages, constraints for the mass flowrate and the pressure ratio are necessary. The mass flowrate in the ADP should be above 0.175 kg/s to reach the design criteria of the heat exchangers and below 0.275 kg/s to satisfy the power consumption limit of the gear system. Furthermore, the pressure ratio of the compressor stage should be above 2.3. The material of rotor and stator will be the titanium alloy Ti-6Al-4V; hence, the stresses in the impeller should be below 600 MPa. Besides the ADP, a highly throttled operating point will be regarded, to ensure a decent distance of the ADP to the surge line. That operating point will be at the same speed line, but with an increased back pressure of 2%. During the optimization, no surge margin distance will be calculated; therefore, no Cumpsty margin is calculated either. For the highly throttled operating point, only the convergence of CFD is required. The objective will be the maximization of the efficiency in the ADP. The initial design does not satisfy the pressure ratio and structural-mechanical needs and is derived from the design of an already existing compressor test rig. The optimization problem can be formulated as

$$\begin{aligned} \text{Minimize Obj} &\equiv -\frac{\eta_{tt}}{\eta_{tt}^{\text{Baseline}}} \\ \text{subject to Constraint 1} &\equiv \frac{\dot{m}}{0.25\,\text{kg/s}} \in [0.7,\ 1.1] \\ \text{Constraint 2} &\equiv \frac{\pi_{ts}}{2.3} \in [1,\ \text{inf}\,] \\ \text{Constraint 3} &\equiv \frac{\sigma_{\text{mises}}}{600\ \text{MPa}} \in [0,\ 1] \\ \text{Constraint 4} &\equiv \text{HTOP CFD converged} \end{aligned} \tag{10}$$

3 Surrogate Models

Gradient-free optimization approaches suffer from low convergence rates; hence, new designs are created by genetic operations like mutation or crossover. To counter this, surrogate models are used. In this section, three different types of surrogate models are presented at a glance. For detailed explanations, as well as implementation strategies, further references in the literature are given.

A classical and well-known surrogate model is the Gaussian process regression, also known as Kriging. In the case of ordinary Kriging, the idea is to approximate the function by the main trend with one regression function combined with a Gaussian random process with zero mean. The covariance of the random process is assumed to be only dependent on the distance of two arguments multiplied by a constant variance. The free parameters of the regression function and of the random process are determined, such that the Kriging model is the best linear unbiased predictor. This process is called the training of the surrogate model. The result is a surrogate model that does not only give predictions of function values but also a value of the variance of the prediction. The variance of the prediction is small in the area of already existing datasets and increases away from it. Based on that, it is possible to define the different infill criteria. The first and very common approach is called *expected improvement* (*E*). The idea is to scan the surrogate model for arguments with the biggest chance of getting better than the current best dataset in the database. Another infill criterion is called *prediction minimization* (*P*), with the goal in only going to minimize the value of the prediction without consideration of the variance. Further information on Kriging surrogate models can be found in Refs. [16,17].

Another surrogate model is called *neural gas* (*N*). The idea is to use self-organizing maps, also known as Kohonen net, which is a kind of artificial neural network. Each neuron of the Kohonen net consists of a weight out of the argument set and a position in a 2-dimensional space. Higher dimensions are also possible. During the training phase, the weights of the neurons are adapted, such that similar samples are located closer and adjective samples far more apart. New samples are generated through the evaluation of the artificial neural network. Further information on neural gas can be found in Ref. [18]. For the optimization process, individual surrogate models are created for the objective and each constraint.

4 Optimization Problem

The optimization process is started with 100 randomly generated geometries based on the baseline geometry. Next, all of the new iterations are generated by surrogate model evaluations. The rotational speed in the ADP is 100.000 rpm. The inlet condition was defined by a total pressure of 3.8 bar and a total temperature of 420.0 K. The infill criteria are selected by a random process with weight w_E for expected improvement, w_P for prediction minimization, and w_N for neural gas. Each weight has to be in $R_+ := [0, \inf)$. The ratio $w_\cdot/(w_E + w_P + w_N)$ describes the probability of selecting the surrogate model $\cdot$. A maximum number of 1500 iterations was used for terminating the optimization process.

4.1 Optimization Results. The first optimization run was conducted with infill criteria probabilities $(w_E, w_P, w_N) = (3, 1, 1)$. Because of the stochastic nature of both the infill criteria selection and the surrogate model structure as well as the evolutionary algorithm for solving the optimization problem, the optimization was repeated five times. The optimization process can be seen in Fig. 13. The figure shows only iterations, that satisfy all of the constraints and have a converged highly throttled operating point. It can be seen that neither the baseline geometry nor one of the 100 randomly generated members for the initial dataset satisfies all of the constraints. Moreover, the first member that fulfills all of the constraints can be found after approximately 300 iterations. Besides the objective decrements, a confidence interval with a 95% level

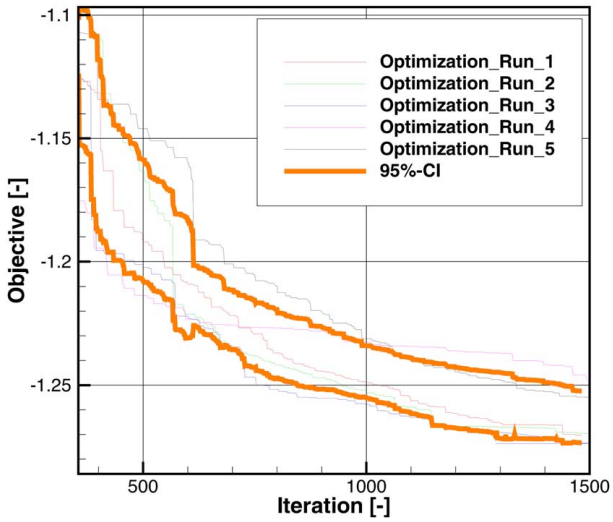

Fig. 13 comparison of three optimization runs with same infill criteria and calculated 95% confidence interval

is shown. It can be seen that the confidence interval is wide in the early phase and narrow in the late phase of the optimization. Possible reasons are the strong dependence of the objective decrement on the infill criteria selection, which is in the early phase very different from the defined selection criteria. During the ongoing optimization, the ratio of the selected infill criteria converges to the predefined probability distribution; hence, the confidence interval decreases. Besides that, all objective decrements are not fully converged within the iteration limit. This motivates to investigate different infill criteria probabilities.

The comprehensive study is shown in Fig. 14. The convergence trajectories with only one kind of surrogate model $(w_E, w_P, w_N) = (0, 0, 1)$, $(w_E, w_P, w_N) = (0, 1, 0)$, and $(w_E, w_P, w_N) = (1, 0, 0)$ are shown with squares as symbol, combinations of two different surrogate models $(w_E, w_P, w_N) = (1, 1, 0)$, $(w_E, w_P, w_N) = (1, 0, 1)$, and $(w_E, w_P, w_N) = (0, 1, 1)$ are visualized by circles and those combining three $(w_E, w_P, w_N) = (3, 1, 1)$, $(w_E, w_P, w_N) = (1, 3, 1)$, and $(w_E, w_P, w_N) = (1, 1, 3)$ are plotted using diamonds. No further combinations were conducted. It can be seen that the convergence behavior of only *N* (squares, resulting in objective value of -1.145) is the least optimal. Similar results can be observed for *P* (squares, resulting in -1.192). Possible reasons are the very exploitative and no explorative strategy of these surrogate models. Only two infill criteria combinations $(w_E, w_P, w_N) = (1, 3, 1)$ and $(w_E, w_P, w_N) = (1, 1, 3)$ reach the best solution with an objective decrement of -1.285. For both trajectories, a good convergence behavior can be noticed. The other combinations of surrogate models perform similarly to the first investigated combination and are in the area of the confidence interval.

Further statistical comparison of three different infill criteria combinations are shown in Fig. 15. Because of limited cluster contingent, only the combinations $(w_E, w_P, w_N) = (3, 1, 1)$, $(w_E, w_P, w_N) = (1, 3, 1)$, and $(w_E, w_P, w_N) = (1, 1, 3)$ are carried out. Each confidence interval was calculated based on five optimizations. It can be clearly seen that the mean of confidence interval of $(w_E, w_P, w_N) = (1, 1, 3)$ is lower than the means of the other confidence intervals. The least optimal mean has a combination $(w_E, w_P, w_N) = (3, 1, 1)$. Furthermore, the width of all three confidence intervals is comparable.

4.2 Result Interpretation. The baseline geometry is compared with the last iteration of the optimization run with infill criteria combination $(w_E, w_P, w_N) = (1, 3, 1)$. The geometry is the same as the result of optimization run with infill criteria combination

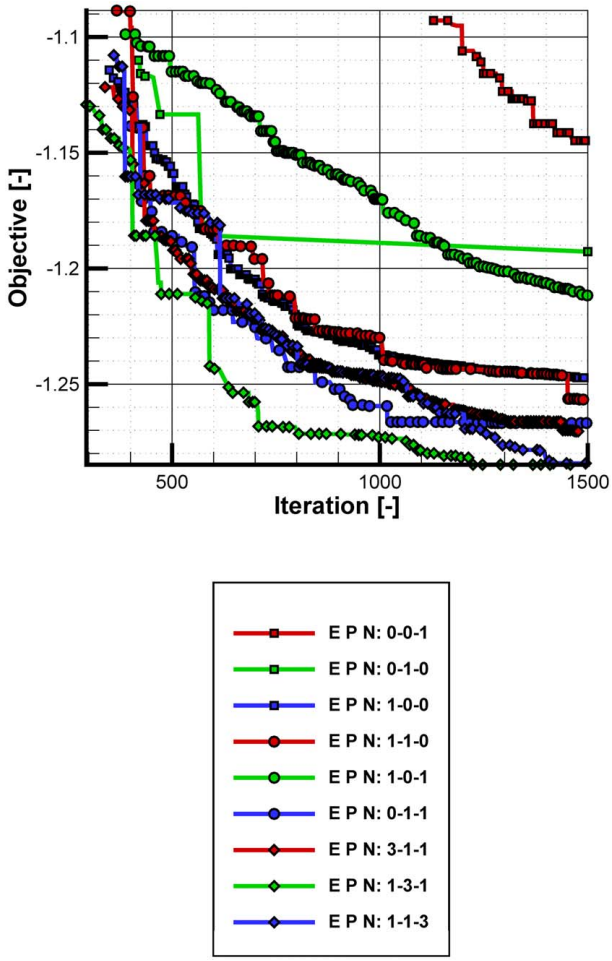

Fig. 14 Convergence history of different combinations of infill criteria

$(w_E, w_P, w_N) = (1, 1, 3)$. The flow path variation and the radial start and end positions of blade and vane can be seen in Fig. 16. Only slight modifications of the flow path can be noticed. The diameter of the impeller was nearly kept constant, but the radial starting position of the vane, which was decreased by free variable

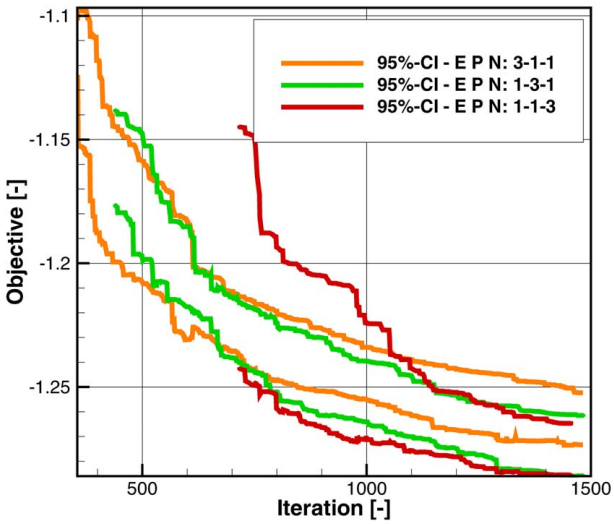

Fig. 15 Comparison of three 95% confidence interval of infill criteria combinations

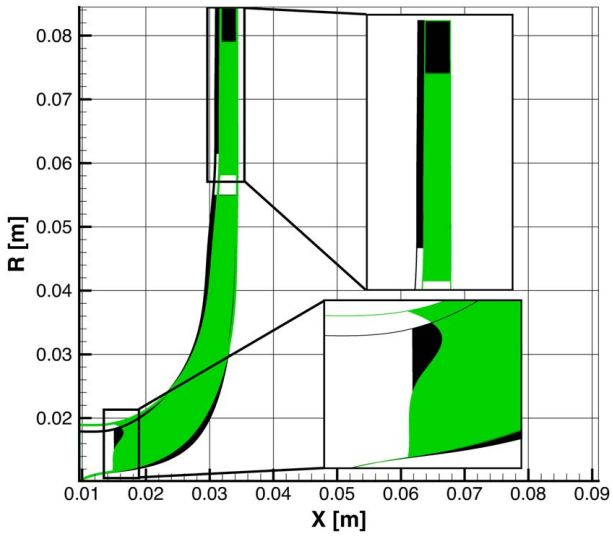

Fig. 16 Baseline geometry (straight leading edge) and optimized flow path (curved leading edge) in meridional plane

#38 : 0.062 → 0.0585 as well as the diameter by free variable #39: 0.084 → 0.0788. The optimizer was able to reach the required pressure ratio without increasing the impeller diameter, which often leads to higher losses due to higher outlet Mach numbers. The decrement of the vaneless space reduces the logarithmic path of the fluid behind the impeller caused by the guided stream path by the vaned diffusor. The reduction of the diffusor diameter reduces friction losses. The optimized disk geometry is shown in Fig. 17. Slight modifications in the rear side can be identified by adapting free variable #35 : 0 → 0.0003. The overall disk thickness was kept constant.

The blade parametrization was highly modified. Figures 18 and 19 show the redesigned inlet geometry with a modified lean angle and the optimized leading edge contour with a one-sided S-shaped contour. The β angle was decreased in the case of the hub surface by free variable #16: −5 deg → −9.98 deg and for the casing by free variable #15: −15 deg → −19.4 deg. The β angles at the trailing edge did not change significantly. The leading edge contour was designed by a huge increment of free variable #9: 0 → 0.2, which is the upper limit for the optimizer. With an increased limit, the optimizer would probably select bigger shifts. The shock losses could be

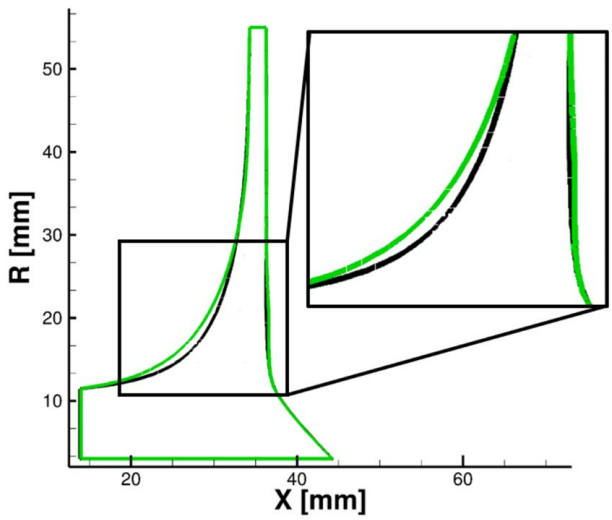

Fig. 17 Baseline and optimized disk geometry in the meridional plane

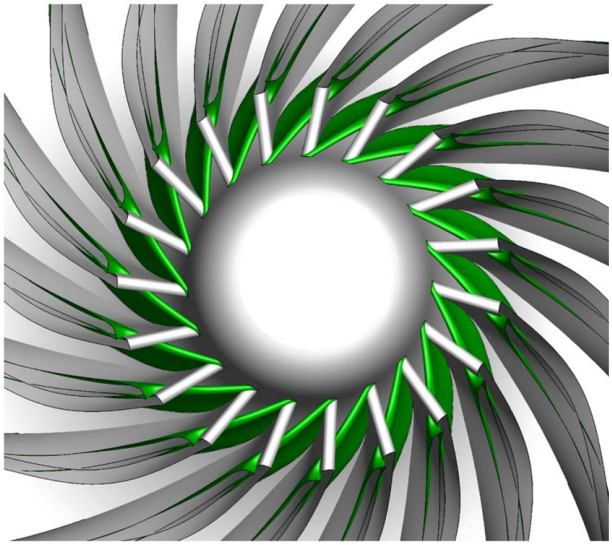

Fig. 18 Comparison of baseline (lean angle 90°C) and optimized (lean angle 45°C) geometry with focus on inlet

significantly avoided by shifting the impeller from a transonic to nearly subsonic behavior. The β angle of the vane was slightly decreased at the leading edge by free variable #27: 83.5 deg → 82.73 deg and at the trailing edge by free variable #28: 69.5 deg → 65.3 deg. The θ angle was reduced by free variable #40: 160 deg → 157.1 deg.

The resulting flow based on the shape modifications can be seen in Fig. 20. The Mach number at 50% span is shown. The flow is successfully decelerated at the inlet and outlet area of the impeller. Additionally, the flow on the suction side is homogenized, which leads to reduced losses due to secondary flow phenomena. The flow in the diffusor passage is kept constant, but with a decreased diffusor diameter, which reduces the friction. A detailed view on the passage flow of the impeller is shown in Fig. 21. It can be seen that the redesigned lean angle of the leading edge and the complex leading edge contour reduce the Mach number significantly. Again, a detailed view of the flow inside the impeller passage is given that shows the deceleration of the flow at the suction side that results in lower flow separation. The comparison of the flow at the outlet of the impeller can be seen in Fig. 22. Due to the optimized rake angle by free variable #25 : 0 → 0.0276, the passage flow is reduced, hence the transformation of kinetic energy to static pressure in the diffusor area is improved.

The aerodynamic loading of the impeller blade at 50% span is shown in Fig. 23. The upper, intersecting lines show the isentropic

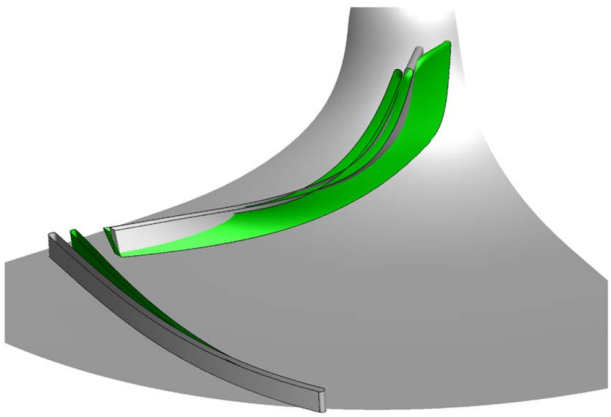

Fig. 19 Single blade and vane comparison of baseline (straight leading edge) and optimized (curved leading edge, reduced vaneless space) geometry

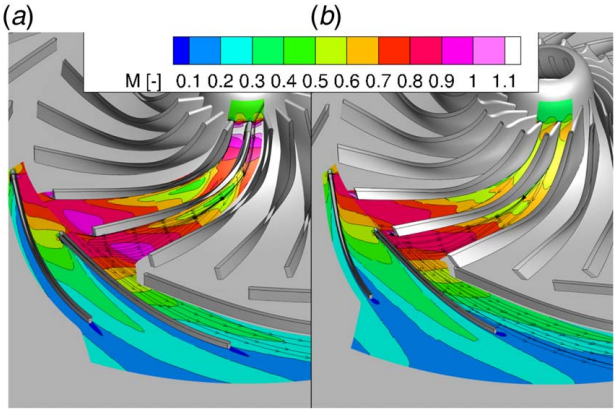

Fig. 20 Flow comparison of absolute Mach number at 50% span between baseline (*a*) and optimized (*b*) geometry

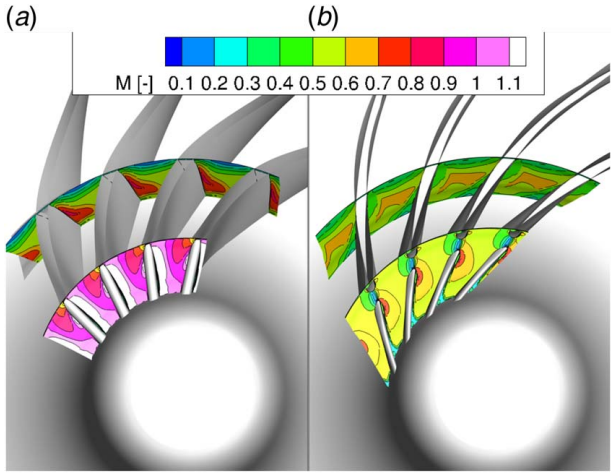

Fig. 21 Comparison of absolute Mach number in passage at inlet and intermediate position between baseline (*a*) and optimized (*b*) geometry

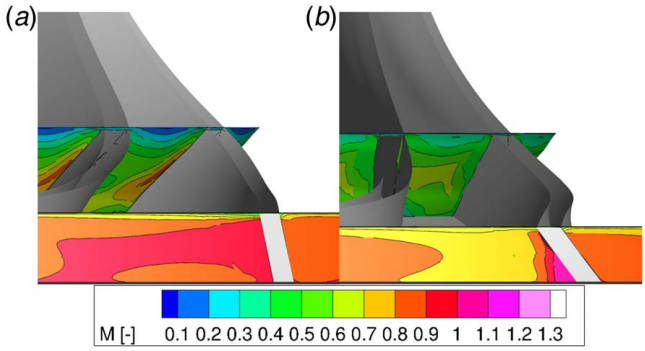

Fig. 22 Comparison of absolute Mach number in passage at impeller outlet between baseline (*a*) and optimized (*b*) geometry

Mach number of the baseline geometry and the loading of the optimized geometry is shown by the lower graphs. Two highlighted areas can be identified with negative loading of the baseline impeller. The optimized geometry has no areas with negative loading. Furthermore, the overall loading behavior is homogenized throughout the blade, which results in higher efficiencies. Furthermore, the Mach number is successfully decreased during the optimization.

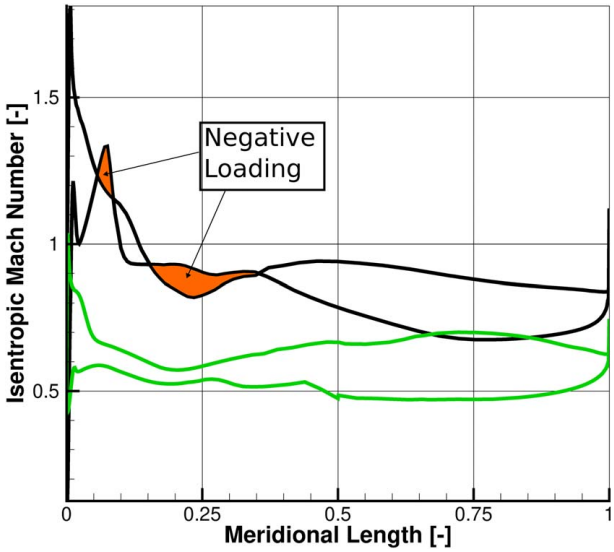

Fig. 23 Comparison of aerodynamic loading of baseline (upper, intersecting lines) and optimized (lower lines) geometry at 50% span

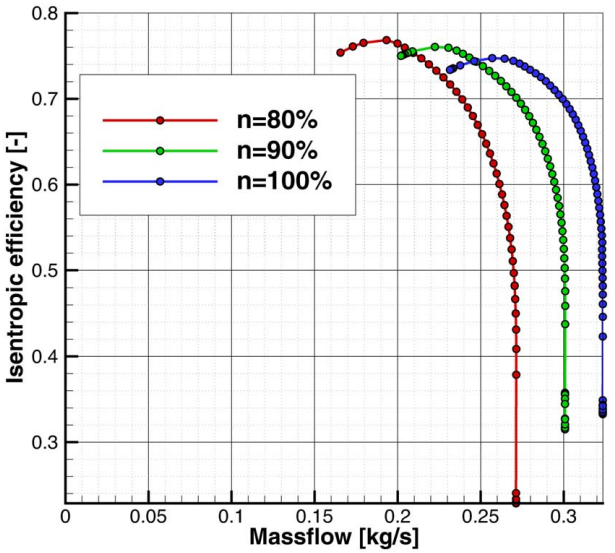

Fig. 25 Performance map with isentropic efficiency of optimized geometry

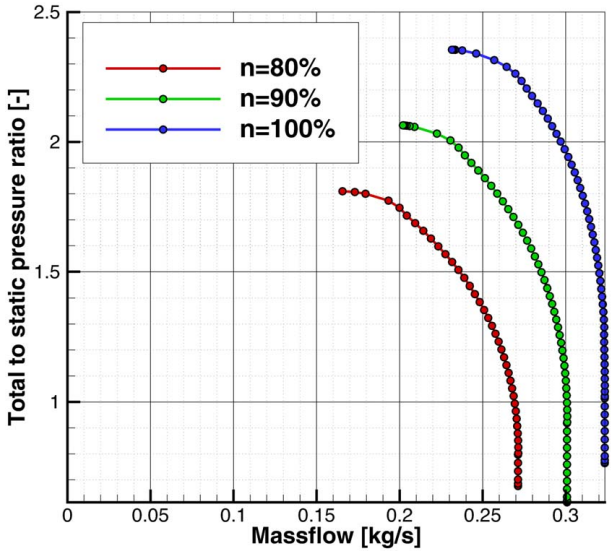

Fig. 24 Performance map with total to static pressure ratio of optimized geometry

The performance map of the radial compressor stage is shown in Figs. 24 and 25. The first figure visualizes the ratio of total and static pressure for three speed lines, starting at $n = 80\%$ up to $n = 100\%$. The ADP with a pressure ratio of 2.3 and a mass flowrate of 0.26 kg/s has a decent distance to the surge line, at the speed line with $n = 100\%$. Without the integration of the highly throttled operating point, the optimizer would possibly shift the ADP up to the surge line. The isentropic efficiency with respect to the mass flowrate is shown in Fig. 25. It can be noticed, that the ADP is at the maximum of the speed line $n = 100\%$. Furthermore, higher efficiencies are possible by reducing the rotation speed of the compressor that leads to lower pressure ratios.

5 Automatic Hyperparameter Tuning

The results of the comprehensive study for different infill criteria combinations shown in Fig. 14 motivate further investigation of the best choice for the values of the model parameters w_E, w_P, and w_N. This is carried out by an AHPT. The hyperparameter tuning is done by an implemented Bayesian optimization approach. The optimization process is supported by a Gaussian process regression surrogate model. Due to the fact that only the ratio of w_E to w_P and w_N are influencing the performance of the optimization process, w_E, w_P, and w_N can be considered in the interval [0, 1] without loss of generality. The optimization process is initialized by two randomly generated samples of model parameter combinations. Further iterations are generated by evaluating the surrogate model. The result of the AHPT is shown in Fig. 26. It can be seen that iteration eight has the lowest objective value and is more optimal than the best found solution within the comprehensive study. An objective value of -1.2918 could be achieved with model parameters $(w_E, w_P, w_N) = (0.344, 0.310, 0.346)$.

The geometry modified by the AHPT is compared with the optimized geometry with infill criteria combination $(w_E, w_P, w_N) = (1, 3, 1)$. Significant changes in the circumferential coordinates, the control points of the β angle distribution, and the control points of the leading edge interpolation were noted. The circumferential coordinate was further optimized by modifying #13: 60.83 deg → 63.00 and #14: 60.00 deg → 57.99. Slight modifications of the

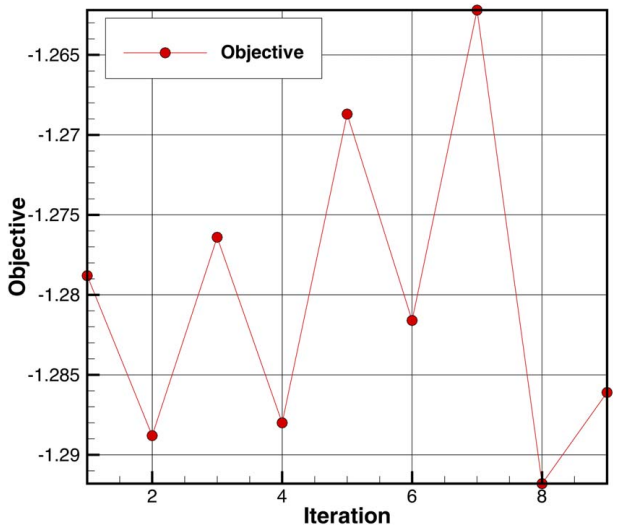

Fig. 26 Convergence history of automatic hyperparameter tuning

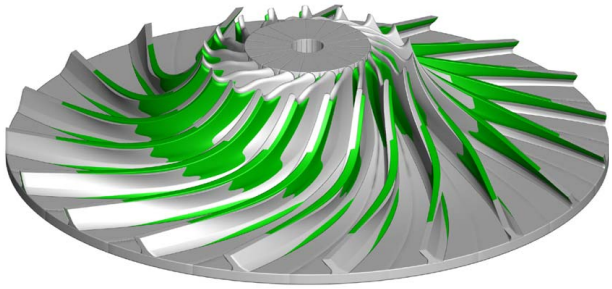

Fig. 27 Comparison of the impeller geometry of automatic hyperparameter tuning and infill criteria combination (w_E, w_P, w_N) = (1, 3, 1)

β angle control points #20 : 0.06 → 0.10, #21 : 0.60 → 0.55, and #22 : 0.073 → 0.032 further optimized the intermediate shape of the impeller geometry. Another modification could be observed of the leading edge control points: #8: −0.033 → −0.076, #9: −0.023 → −0.013, #10: 0.028 → 0.060, and #12: −0.10 → 0.024. The resulting geometry of the AHPT and the geometry with the model parameters (w_E, w_P, w_N) = (1, 3, 1) is shown in Fig. 27.

6 Conclusion

The article presents an aerodynamic optimization for a radial compressor stage with application in an HTHP test rig. The working fluid is water steam. The rotational speed was kept constant at 100,000 rpm.

The optimization was done by a gradient-free algorithm, that is accelerated by surrogate models. The blade and vane are parametrized by 40 free variables. A highly throttled operating point is regarded, to achieve a descent distance of the ADP to the surge line. Three different surrogate models and infill criteria were investigated. The best combination of infill criteria was found to be (w_E, w_P, w_N) = (1, 3, 1) and (w_E, w_P, w_N) = (1, 1, 3).

The optimized geometry satisfies all constraints. The required pressure ratio of 2.3 could be realized. An isentropic efficiency of nearly 75% in the ADP for the compressor stage was calculated. The effect of negative loading could be successfully avoided in the optimized impeller geometry.

Furthermore, an automated hyperparameter tuning was carried out to investigate the most optimal combination of infill criteria. The result was a geometry with an improved isentropic efficiency of about 0.68 percentage points compared to the result of the optimization with (w_E, w_P, w_N) = (1, 3, 1).

Finally, the optimized compressor stage was analyzed in terms of aerodynamic performance. Special features, like β angle, rake angle, and leading-edge contour were described quantitatively. During the optimization, the leading-edge parametrization reached the parameter limit. Further optimization with refined leading edge control points could generate more optimal solutions. That will be investigated in the next design steps of turbocompressors for HTHP.

Acknowledgment

We would like to thank the DLR, Energy Programme Directorate for its support and the unknown reviewers for their useful suggestions.

Conflict of Interest

There are no conflicts of interest.

Data Availability Statement

The datasets generated and supporting the findings of this article are obtainable from the corresponding author upon reasonable request.

Nomenclature

h = Spatial discretization
m = Meridional coordinate
n = Rotational speed (1/min)
r = Radial coordinate (m)
r = Refinement ratio
p = Order of convergence
E = Discretization error
M = Mach number
S = Meridional length
$\dot{m}$ = Mass flowrate (kg/s)
w_E = Weight of expected improvement
w_N = Weight of neural gas
w_P = Weight of prediction minimization
m' = Normalized meridional coordinate

Greek Symbols

β = Beta angle of blade (deg)
γ = Rake angle (deg)
η = Isentropic efficiency (%)
θ = Circumferential coordinate (deg)
π = Pressure ratio
σ = Von Mises stress (MPa)

Superscripts and Subscripts

ts = Total to static property
tt = Total to total property

Abbreviations

ADP = Aerodynamic design point
AHPT = Automatic hyperparameter tuning
AR = Asymptotic range
CFD = Computational fluid dynamic
CSM = Computational structure mechanics
E = Expected improvement
GCI = Grid convergence index
HTHP = High-temperature heat pump
HTOP = Highly throttled operating point
N = Neural gas
P = Prediction minimization

References

[1] Pörtner, H.-O., Roberts, D. C., Poloczanska, E. S., Mintenbeck, K., Tignor, M., Alegría, A., Craig, M. et al., 2022, "Introduction," *Climate Change 2022: Impacts, Adaptation, and Vulnerability. Contribution of Working Group II to the Sixth Assessment Report of the Intergovernmental Panel on Climate Change*, H.-O. Pörtner, D. C. Roberts, M. Tignor, E. Poloczanska, K. Mintenbeck, A. Alegría, M. Craig et al., eds., Cambridge University Press, UK, pp. 3–33.

[2] Meroni, A., Zühlsdorf, B., Elmegaard, B., and Haglind, F., 2018, "Design of Centrifugal Compressors for Heat Pump Systems," Appl. Energy, **232**, pp. 139–156.

[3] Schiffmann, J., 2015, "Integrated Design and Multi-Objective Optimization of a Single Stage Heat-Pump Turbocompressor," ASME J. Turbomach., **137**(7), p. 071002.

[4] Casey, M., and Robinson, C., 2021, *Radial Flow Turbocompressors: Design, Analysis, and Applications*, Cambridge University Press, UK.

[5] Goinis, G., 2020, *Gehäusestrukturierungen für transsonische Verdichter*, Dissertation. Ruhr-Universität Bochum. Thesis.

[6] Raitor, T., Reutter, O., Aulich, M., and Nicke, E., 2013, "Aerodynamic Design Studies of a Transonic Centrifugal Compressor Impeller Based on Automatic 3D-CFD Optimization," 10th European Turbomachinery Conference, Lappeenranta, Finland, Apr. 15–19.

[7] Cumpsty, N., 2004, *Compressor Aerodynamics*, Vol. No. Bd. 10, Krieger Publishing, Toledo, OH.

[8] Ratz, J., Leichtfuß, S., Beck, M., Schiffer, H.-P., and Fröhlig, F., 2019, "Surge Margin Optimization of Centrifugal Compressors Using a New Objective Function Based on Local Flow Parameters," Int. J. Turbomach., Propul. Power, **4**(4), p. 42.

[9] Van Den Braembussche R, R. A., 2006, *Optimization of Radial Impeller Geometry*, RTO-VKI Lecture Series on High Speed Pumps.

[10] Hiradate, K., Kanno, T., Nishida, H., Shinkawa, Y., and Joukou, S., 2010, "Improvement in Efficiency and Operating Range of Centrifugal Blower Stage for Sewage Aeration Blower," Int. J. Fluid Mach. Syst., **3**(4), pp. 379–385.
[11] Châtel, A., and Verstraete, T., 2022, "Aerodynamic Optimization of the SRV2 Radial Compressor Using an Adjoint-Based Optimization Method," ASME Turbo Expo 2022: Turbomachinery Technical Conference and Exposition, Rotterdam, June 13.
[12] Voß, C., Aulich, M., and Raitor, T., 2014, "Metamodel Assisted Aeromechanical Optimization of a Transonic Centrifugal Compressor," ISROMAC 15, Honolulu, HI, Feb. 24–28.
[13] Aulich, M., Voß, C., and Raitor, T., 2024, "Optimization Strategies demonstrated on a Transonic Centrifugal Compressor," ISROMAC, Honolulu, HI, Feb. 24.
[14] Hottois, R., Châtel, A., Coussement, G., Debruyn, T., and Verstraete, T., 2022, "Comparing Gradient-Free and Gradient-Based Multi-Objective Optimization Methodologies on the VKI-LS89 Turbine Vane Test Case," ASME J. Turbomach., **145**(3), p. 031001.
[15] Hehn, A., Mosdzien, M., Grates, D., and Jeschke, P., 2018, "Aerodynamic Optimization of a Transonic Centrifugal Compressor by Using Arbitrary Blade Surfaces," ASME J. Turbomach., **140**(5), p. 051011.
[16] Aissa, M. H., and Verstraete, T., 2019, "Metamodel-Assisted Multidisciplinary Design Optimization of a Radial Compressor," Int. J. Turbomach. Propul. Power, **4**(4), p. 35.
[17] Schmitz, A., 2020, *Multifidelity-Optimierungsverfahren für Turbomaschinen*, Dissertation. Ruhr Universität Bochum. 193 S.
[18] Martinetz, T., and Schulten, K., 1991, "A Neural-Gas Network Learns Topologies," Artif. Neural Netw., **1**, pp. 397–402.
[19] Voß, C., and Nicke, E., 2008, *Automatische Optimierung von Verdichterstufen*, Berichtsreihe (DLR-Forschungsbericht).
[20] Drela, M., and Youngren, H., 2022, "A User's Guide to MISES 2.63," Version 2.63, MIT Aerospace Computational Design Laboratory, https://web.mit.edu/drela/Public/web/mises/mises.pdf, Accessed December 20, 2022.
[21] Sauer, M., 2018, "An Optimization Based Approach to Multi-Block Structured Grid Generation," 6th European Conference on Computational Mechanics, Glasgow, UK, June 11–15.
[22] Slater, J. W., 2022, "Examining Spatial (Grid) Convergence," Version 1.0, National Aeronautics and Space Administration, https://www.grc.nasa.gov/WWW/wind/valid/tutorial/spatconv.html, Accessed November 29, 2022.
[23] Roache, P. J., 1994, "Perspective: A Method for Uniform Reporting of Grid Refinement Studies," ASME J. Fluids Eng., **116**(3), pp. 405–413.
[24] Franke, M., Kügeler, E., and Nürnberger, D., 2005, "Das DLR-verfahren trace: Moderne simulationstechniken für turbomaschinenströmungen," *Deutscher Luft- und Raumfahrtkongress 2005*, DGLR, ed.
[25] Dhondt, G., 2022, "CalculiX - A Free Software Three-Dimensional Structural Finite Element Program," Version 2.19, http://www.calculix.de/, Accessed December 1, 2022.